AGU PUBLICATIONS

JGR

Journal of Geophysical Research: Solid Earth

RESEARCH ARTICLE

10.1002/2014JB011068

This article is a companion to *Hier-Majumder and Drombosky* [2015], doi:10.1002/2014JB011454.

Key Points:
- Contiguity becomes anisotropic by deformation
- Fast multipole boundary element method
- Nonlinear evolution of anisotropy

Correspondence to:
S. Hier-Majumder,
Saswata.Hier-Majumder@rhul.ac.uk

Citation:
Drombosky, T., and S. Hier-Majumder (2015), Development of anisotropic contiguity in deforming partially molten aggregates: 1. Theory and fast multipole boundary elements method, *J. Geophys. Res. Solid Earth*, *120*, 744–763, doi:10.1002/2014JB011068.

Received 24 FEB 2014
Accepted 18 SEP 2014
Accepted article online 24 SEP 2014
Published online 3 FEB 2015

Development of anisotropic contiguity in deforming partially molten aggregates: 1. Theory and fast multipole boundary elements method

Tyler Drombosky[1] and Saswata Hier-Majumder[2]

[1] Applied Mathematics and Scientific Computation, University of Maryland, College Park, Maryland, USA, [2] Department of Earth Sciences, Royal Holloway, University of London, Egham, UK

Abstract The microstructure of partially molten rocks strongly influences the macroscopic physical properties. Contiguity, a geometric parameter, is a tensorial quantity that describes the area fraction of intergranular contact in a partially molten aggregate. It is also a key parameter that controls the effective elastic strength of the grain network. As the shape of the grains evolves during deformation, so does the contiguity of each grain. In this article, we present the first set of numerical simulations of evolution of grain-scale contiguity of an aggregate during matrix deformation using a fast multipole boundary elements method-based model. We simulate a pure shear deformation of an aggregate of 1200 grains up to a shortening of 0.47 and a simple shear deformation of 900 grains up to a shear strain of 0.75, for solid-melt viscosity ratios of 1 and 50. Our results demonstrate that the initially isotropic contiguity tensor becomes strongly anisotropic during deformation. We also observe that the differential shortening, the normalized difference between the major and minor axes of grains, is inversely related to the ratio between the principal components of the contiguity tensor. In pure shear, the principal components of the contiguity tensor remain parallel to the irrotational principal axes of the applied strain. In simple shear, however, the principal components of the contiguity tensor rotate continually during the course of deformation in this study. In the companion article we present the seismic anisotropy resulting from the anisotropic contiguity and the implications for the Earth's lithosphere-asthenosphere boundary.

1. Introduction

The geometry of melt distribution in partially molten rocks strongly influences their effective physical properties such as elastic moduli, viscosity, electrical conductivity, permeability, and mechanical absorption. At the grain scale, contiguity, the fractional area of intergranular contact, determines the strength of the load-bearing network of grains in the aggregate. The contiguity tensor, $\boldsymbol{\psi}$, is described as a function of the intergranular contact function, χ, and the normal to the grain boundary, $\hat{\boldsymbol{n}}$, as,

$$\boldsymbol{\psi} = \frac{1}{l}\int_{\Gamma} \chi\, \hat{\boldsymbol{n}}\hat{\boldsymbol{n}}\, \mathrm{d}\Gamma, \tag{1}$$

where l is the length of the grain boundary in 2-D and the integral is taken over the entire grain boundary, Γ. The spatially variable contact function assumes a value of unity at grain-grain contacts and zero at grain-melt contact.

For a given volume fraction of melt and a given melt-grain dihedral angle, the contiguity of the aggregate depends on the state of deformation [*Takei and Holtzman*, 2009; *Takei*, 2005]. For example, in an undeformed aggregate, a small volume fraction of melt can be distributed in randomly oriented grain-edge tubules. Deformation of such an aggregate will redistribute the same volume fraction of melt into grain boundary films [*Hier-Majumder and Kohlstedt*, 2006; *Zimmerman et al.*, 1999; *Daines and Kohlstedt*, 1997] or melt-rich, disaggregated bands [*Holtzman et al.*, 2003; *Hustoft and Kohlstedt*, 2006; *King et al.*, 2011]. As the melt preferentially wets some grain boundaries, the contact function deviates from the undeformed state, inducing a change in the values of the components of the contiguity tensor. The orientation of these newly created melt films and bands will be governed by the orientation of the principal stresses, rendering the contiguity tensor anisotropic. Since the elastic strength of the network of grains is controlled by the contiguity of the aggregate, the development of anisotropic contiguity will be reflected in a change of the elastic properties of the aggregate.

Forces arising from plate tectonics can be agents of such textural transformation in the Earth's interior. One especially interesting region is the lithosphere-asthenosphere boundary (LAB), characterized by a large reduction of the strength of the asthenosphere underlying the rigid lithosphere. Besides the reduction in strength, the LAB is marked by a sharp reduction [*Fischer et al.*, 2010; *Rychert et al.*, 2010; *Schmerr*, 2012] and a global anisotropy [*Nettles and Dziewoński*, 2008; *Beghein et al.*, 2014] in shear wave speed, anisotropic electrical conductivity [*Naif et al.*, 2013; *Evans et al.*, 2005], and a small volume fraction of melt [*Sifré et al.*, 2014]. The LAB is also a dynamic environment as the motion between rigid plates and the flow in the weak asthenosphere are coupled through this region. Deformation of the partially molten matrix of the LAB will segregate the melt, rendering the contiguity anisotropic. The coupling between deformation and anisotropic contiguity, therefore, provides an important set of constraints to explain the observed features of the LAB. To quantify this coupling, laboratory experiments and theoretical models of microstructures serve as powerful tools.

The role of deformation in melt redistribution has been studied extensively in laboratory experiments [*Daines and Kohlstedt*, 1997; *Holtzman et al.*, 2003; *Hustoft and Kohlstedt*, 2006; *Hier-Majumder and Kohlstedt*, 2006; *Zimmerman et al.*, 1999; *Takei*, 2005; *King et al.*, 2011]. In these two-step experiments, the first step involved preparing undeformed, hot isostatically pressed aggregates. Next, these aggregates were deformed in pure shear, simple shear, or torsion configurations. After deformation, melt segregation was characterized by comparing microstructures of undeformed and deformed samples. While the melt geometry before and after deformation could be measured from these experiments, the experimental setup precluded the possibility of monitoring the evolution of contiguity during the course of deformation. In addition, *Takei* [2005] studied the development of shear wave anisotropy caused by the development of anisotropic contiguity during deformation experiments on analogue materials. While the results from these laboratory experiments indicate a likely relation between them, a direct quantification linking deformation, anisotropic contiguity, and anisotropic shear wave speed is still lacking.

Theoretical models of microstructure follows two different approaches. The first approach uses grain-melt geometry based on an assumed steady state grain shape [*von Bargen and Waff*, 1986; *Wray*, 1976; *German*, 1985; *Takei*, 1998]. The work of *Takei* [1998] introduced the use of contiguity in the constitutive relations of partially molten rocks. The contiguity in this work, however, was derived by varying the size of intergranular contact patches on the surface of a spherical grain. Since the description of contiguity is purely geometric, this group of formulations fail to account for the role of deformation in the evolution of contiguity. To address this issue, a second group of models, termed microgeodynamic models, presented a formulation for simulating the equilibrium geometry of partially molten aggregates driven by surface tension and small viscous deformation within the grains [*Hier-Majumder*, 2008, 2011; *Hier-Majumder and Abbott*, 2010; *Wimert and Hier-Majumder*, 2012]. Using the boundary elements method (BEM) and a semianalytical method, this group of articles quantified the contiguity of a unit cell in a partially molten aggregate for varying surface tensions in the steady state.

The BEM, while containing the equations necessary to describe the microstructure at large strains, suffered from a limitation. In the BEM, the governing partial differential equations (PDEs) of mass and momentum conservation are converted to a Boundary Integral Equation (BIE). When this BIE is discretized into a set of algebraic equations for numerical solution, the resulting system of algebraic equations is dense. As a result, calculations involving many grains become prohibitively expensive. This issue limited the capacity of these models in addressing the role of deformation in the development of anisotropic contiguity. It is crucial to incorporate a large number of grains in microstructural simulations of deformation such that melt segregation over length scales larger than a unit cell can be modeled. Thus, it is necessary to develop a numerical technique that can address the crucial issues of measuring anisotropic contiguity during deformation and yet remain computationally feasible.

This work bridges the gap by implementing the Fast Multipole Method (FMM) to numerically accelerate the BEM. We employ the resulting Fast Multipole Boundary Elements Method (FMBEM) to study the development of anisotropic contiguity in deforming partially molten rocks. This model tracks the evolution of anisotropic contiguity and anisotropic shear wave speed as deformation progresses. To the best of our knowledge, this is the first study that directly quantifies the link between deformation, development of anisotropic contiguity, and anisotropic shear wave speeds.

We present our results in two articles. This article outlines numerical methods and presents the simulated microstructures for pure and simple shear deformation. The companion article by *Hier-Majumder and Drombosky* [2015, labeled HMD] presents the results for anisotropic contiguity and anisotropic shear wave velocity and the implications for the observed nature of the LAB. We introduce the various aspects of our mathematical model in section 2. We present the governing PDEs and the BIE in this section. The section also includes a mathematical description of the problem geometry and computation of differential shortening and the contiguity tensor. In section 2.4, we develop the numerical methods involving FMM numerical acceleration technique. In section 2.5, we present a perturbation analysis for the steady state shape of an isolated grain. Section 3 presents the results of our numerical simulations. In section 4, we discuss the trade-offs involved in our selection of parameter space and provide a qualitative comparison between our work and previous studies. Summary and conclusions of the microstructural model are provided in section 5.

2. Model

The evolution of the melt geometry in a deforming, partially molten aggregate is determined by a coupled viscous flow within the grains and melt. In this section we present the governing equations for the coupled flow, the setup for our numerical simulations, and the methods of postprocessing our numerical data.

2.1. Governing Equations

Consider a collection of viscous, contiguous grains with the interstitial space filled with a less viscous melt. The grains and melt are treated as incompressible fluids, such that the conservation of mass within each phase leads to

$$\nabla \cdot \boldsymbol{u}^P = 0, \tag{2}$$

where the superscript $P = 1, \ldots, N+1$ for a collection of N grains and the interstitial melt and $\boldsymbol{u}^P$ is the velocity of the Pth phase. Balance of force within each grain and the melt requires that, in the absence of a body force,

$$\nabla \cdot \mathbf{T}^P = 0, \tag{3}$$

where the stress tensor $\mathbf{T}^P$ for a phase with viscosity μ^P and dynamic pressure p^P is given by,

$$\mathbf{T}^P = -p^P \mathbf{I} + \mu^P \left(\nabla \boldsymbol{u}^P + \left(\nabla \boldsymbol{u}^P \right)^T \right), \tag{4}$$

where $\mathbf{I}$ is the unit tensor and the second term on the right-hand side is the symmetric velocity gradient tensor. The governing PDEs (2) and (3) within each grain and the melt need to be supplemented with boundary conditions to solve for the unknown velocity and dynamic pressure.

First, we impose the no-slip boundary condition at the surface, Γ_P, of each of the N grains [*Pozrikidis*, 2001; *Leal*, 1992; *Kim and Karilla*, 2005], such that

$$\Delta \boldsymbol{u} \mid_{\Gamma_P} = 0, \tag{5}$$

where $\Delta \boldsymbol{u}$ is the difference between the velocity within the grain and the melt at the Γ_P grain surface.

Next, we require that the difference in traction across the grain interface is balanced by surface tension forces, leading to the vector boundary condition on Γ_P

$$\Delta \mathbf{T}^P \cdot \hat{\boldsymbol{n}} + \left(\mathbf{I} - \hat{\boldsymbol{n}}\hat{\boldsymbol{n}} \right) \nabla \gamma - \gamma \hat{\boldsymbol{n}} \nabla \cdot \hat{\boldsymbol{n}} \mid_{\Gamma_P} = 0, \tag{6}$$

where $\Delta \mathbf{T}^P$ is the stress drop across the surface of the Pth grain, γ is the interfacial tension, and $\hat{\boldsymbol{n}}$ is the unit normal vector along Γ_P pointing into the melt [*Leal*, 1992]. The first term in (6) arises from the difference in the traction across the grain-melt interface. The second term, often described as the Marangoni condition, arises due to the variation of surface tension along the interface of the grain. The tensor operator, $\mathbf{I} - \hat{\boldsymbol{n}}\hat{\boldsymbol{n}}$, projects the vector gradient of surface tension on the interface of the grain. As a result, this component of the boundary condition is tangential to the boundary. The final term, often described as the Laplace condition, arises from curvature-driven surface tension force, where the principle curvature of the interface is

given by $\nabla \cdot \hat{\boldsymbol{n}}$ [*Leal*, 1992; *Pozrikidis*, 2001; *Kim and Karilla*, 2005; *Manga and Stone*, 1993]. This term is directed along the unit normal. In the absence of deformation ($\Delta \mathbf{T}^P = \Delta p \mathbf{I}$, from equation (6)) and constant surface tension ($\nabla \gamma = 0$), equation (6) reduces to the Young-Laplace equation [*Kang*, 2005, equation 2.19].

In this work, we assume that the microstructure is equilibrated prior to deformation, and consider the surface tension to be constant along the grain. Laboratory experiments on a number of different grain-melt aggregates with varying dihedral angles reveal that melt segregation during deformation is independent of the dihedral angle [*Hier-Majumder and Kohlstedt*, 2006; *Hustoft and Kohlstedt*, 2006; *Zimmerman et al.*, 1999]. The assumption $\nabla \gamma = 0$, therefore, simplifies our governing equations without introducing a substantial error in the results.

Finally, we need an additional equation to describe the shape of the grain-melt boundary due to deformation. Let $F^P(\boldsymbol{x}, t) = 0$ be the level set that defines Γ_P at time t. To ensure that the volume of each grain remains constant during deformation of the grain, we use the kinematic equation

$$\frac{\partial F^P}{\partial t}(\boldsymbol{x}, t) + \boldsymbol{u}^P(\boldsymbol{x}, t) \cdot \nabla F^P = 0. \tag{7}$$

In the BEM, we eliminate the dynamic pressure, p, by combining the PDEs (2) and (3), subject to the boundary conditions for no-slip (5) and the continuity of traction (6) [*Hier-Majumder*, 2008]. This results in an integral equation for the unknown velocity. For an aggregate containing P grains embedded in a melt, the velocity $\boldsymbol{u}^q(\boldsymbol{x}_0)$ at point $\boldsymbol{x}_0$ on the surface of the qth grain is given by the following:

$$\boldsymbol{u}^q(\boldsymbol{x}_0) = \frac{2}{1+\lambda_q}\left[\boldsymbol{u}^\infty(\boldsymbol{x}_0) - \frac{1}{4\pi\mu_m}\sum_P \int_{\Gamma_P} \Delta \boldsymbol{f}(\boldsymbol{x}) \cdot \boldsymbol{\mathcal{U}}(\boldsymbol{x}, \boldsymbol{x}_0)\, \mathrm{d}\Gamma_P + \sum_P \frac{1-\lambda_P}{4\pi} \int_{\Gamma_P} \boldsymbol{u}(\boldsymbol{x}) \cdot \boldsymbol{\mathcal{T}}(\boldsymbol{x}, \boldsymbol{x}_0) \cdot \hat{\boldsymbol{n}}\, \mathrm{d}\Gamma_P\right], \tag{8}$$

where $\boldsymbol{x}_0$ is often called the "pole point" and the point $\boldsymbol{x}$ on the surface of the Pth grain is called the "field point" [*Pozrikidis*, 2001]. The two integrals over the interface of the Pth grain, Γ_P, are referred to as the "single-layer" and "double-layer" integrals, respectively. The dimensionless parameter, $\lambda_P = \mu_P/\mu_m$, is the viscosity ratio between the Pth grain and melt. The velocity $\boldsymbol{u}^\infty(\boldsymbol{x}_0)$ represents an applied far-field velocity. By prescribing different far-field velocities we can simulate the effect of different environments of deformation of the matrix. This issue is discussed in further detail in the following section. The presence of the unknown $\boldsymbol{u}$ in the integrand of the double layer integral renders equation (8) a Fredholm integral equation of the second kind. Since the integrals on the right-hand side arise from summation over all grains, the system of algebraic equations resulting from the discretization of the BIE is dense. In reality, the influence of faraway grains on the boundary velocity is small. The resulting dense system of discretized equations can be reduced largely by using the fast multipole expansions. We discuss the implementation of this technique in section 2.4.

Both integrands on the right-hand side of equation (8) contain tensorial kernel functions. These tensors $\boldsymbol{\mathcal{U}}(\boldsymbol{x}, \boldsymbol{x}_0)$ and $\boldsymbol{\mathcal{T}}(\boldsymbol{x}, \boldsymbol{x}_0)$ arise from the velocity and stress components of the fundamental solution to the PDE governing Stokes flow [*Pozrikidis*, 2001; *Ladyzhenskaya*, 1963; *Kim and Karilla*, 2005]. For the present two-dimensional analysis, the second rank tensor $\boldsymbol{\mathcal{U}}(\boldsymbol{x}, \boldsymbol{x}_0)$, also referred to as the Stokeslet, is given by

$$\boldsymbol{\mathcal{U}}(\boldsymbol{x}, \boldsymbol{x}_0) = -\mathbf{I} \ln r + \frac{\hat{\boldsymbol{x}}\hat{\boldsymbol{x}}}{r^2}, \tag{9}$$

where $\hat{\boldsymbol{x}} = \boldsymbol{x} - \boldsymbol{x}_0$ and $r = |\hat{\boldsymbol{x}}|$. The third rank tensor $\boldsymbol{\mathcal{T}}(\boldsymbol{x}, \boldsymbol{x}_0)$ is known as the Stresslet and is given by the triad

$$\boldsymbol{\mathcal{T}}(\boldsymbol{x}, \boldsymbol{x}_0) = -4\frac{\hat{\boldsymbol{x}}\hat{\boldsymbol{x}}\hat{\boldsymbol{x}}}{r^4}, \tag{10}$$

When $\boldsymbol{x} \to \boldsymbol{x}_0$, both $\boldsymbol{\mathcal{U}}(\boldsymbol{x}, \boldsymbol{x}_0)$ and $\boldsymbol{\mathcal{T}}(\boldsymbol{x}, \boldsymbol{x}_0)$ diverge while the integrals remain finite in a Cauchy principal value sense [*Pozrikidis*, 2001; *Ladyzhenskaya*, 1963; *Kim and Karilla*, 2005].

The interfacial tension $\Delta \boldsymbol{f}(\boldsymbol{x})$ in the single-layer integral arises from the boundary condition balancing the stress drop across the grain-melt interface with the Laplace and Marangoni conditions. Based on the discussion following equation (6), we drop the Marangoni term such that the interfacial tension becomes

$$\Delta \boldsymbol{f}(\boldsymbol{x}) = \gamma \hat{\boldsymbol{n}} \left(\nabla \cdot \hat{\boldsymbol{n}}\right). \tag{11}$$

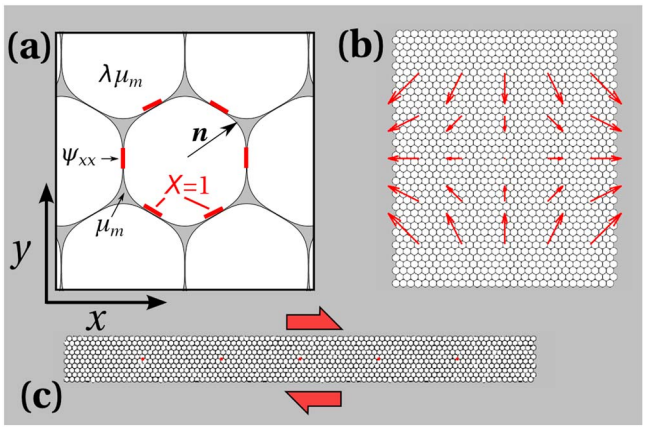

Figure 1. Setup for numerical simulations. (a) Initial geometry of a grain surrounded by six other grains and interstitial melt in gray at three grain junctions. The unit normal to the grain interface $\hat{n}_k(\boldsymbol{x})$, the contact function χ, and the ψ_{xx} component of the contiguity tensor are also shown in the diagram. Viscosity of the melt is μ_m, while that of the grain is $\lambda\mu_m$. (b) The initial configuration of the entire aggregate prior to the pure shear experiment. The aggregate consists of 1200 grains arranged in 40 rows and 30 columns. The red lines indicate the imposed external flow. (c) The initial configuration for simple shear experiment. The aggregate consists of 900 grains arranged in 10 rows and 90 columns. The sense of applied shear, as depicted by the bold red arrows is dextral.

We nondimensionalize the governing equations by the grain radius x_c, velocities by a characteristic velocity scale u_c, and the surface tension by γ_c. We rewrite (8) in dimensionless form yielding

$$\boldsymbol{u}^q(\boldsymbol{x}_0) = \frac{2}{1+\lambda_q}\left[\boldsymbol{u}^\infty(\boldsymbol{x}_0) - \frac{1}{4\pi Ca}\sum_P \int_{\Gamma_P} \Delta\boldsymbol{f}(\boldsymbol{x})\cdot\boldsymbol{\mathcal{U}}(\boldsymbol{x},\boldsymbol{x}_0)\,\mathrm{d}\Gamma_P + \sum_P \frac{1-\lambda_P}{4\pi}\int_{\Gamma_P}\boldsymbol{u}(\boldsymbol{x})\cdot\boldsymbol{\mathcal{T}}(\boldsymbol{x},\boldsymbol{x}_0)\cdot\hat{\boldsymbol{n}}\,\mathrm{d}\Gamma_P\right], \tag{12}$$

where the nondimensional capillary number, Ca, represents the ratio between viscous forces on a grain and the forces arising from surface tension at the grain-melt interface. The capillary number can be expressed in terms of the melt viscosity μ_m, characteristic velocity u_c, and characteristic surface tension γ_c as

$$Ca = \frac{\mu_m u_c}{\gamma_c}. \tag{13}$$

The viscosity ratio between the grain and the melt, and the capillary number are the two parameters that control the evolution of grain shapes for an imposed velocity $\boldsymbol{u}^\infty(\boldsymbol{x}_0)$. At each time step we solve the BIE (12) numerically to obtain the velocities at the boundary nodes of each grain. Then we update the shape of each grain using equation (7). During each time step, we used an arc length-parameterized cubic spline interpolation for the location of quadrature points within each boundary element. From the known coefficients of the cubic spline interpolation, we directly calculated the normal and tangent vectors and the curvature at each quadrature point. These values were then used to determine the boundary velocities from the BIE in the next time step.

2.2. Setup for Numerical Simulations

To study the evolution of anisotropic contiguity by deformation, we carried out two sets of numerical simulations. In each set of simulation, the undeformed aggregate consists of a matrix packed with rounded hexagonal grains surrounded by six neighbors. The simulated microstructure in Figure 1a outlines the geometry of a typical undeformed grain. Following *Hier-Majumder* [2008], the initial grain shape $F^{(P)}(0,\boldsymbol{x}) = 0$ is prescribed by the parametric representation,

$$\boldsymbol{x} = \begin{bmatrix}\cos(\theta)\\ \sin(\theta)\end{bmatrix}(1-\epsilon\cos^2(3\theta)), \tag{14}$$

where θ is the counterclockwise angle from the positive x axis and the constant parameter $\epsilon = 0.05$ represents deviation of an individual grain shape from a unit circle [*Hier-Majumder*, 2008]. The sixfold symmetry of contact patches for each grain is simulated by using the quantity multiplied by ϵ in the above equation.

We want to simulate the response of the partially molten system under an applied, constant strain rate, $\dot{\mathbf{E}}$. This is achieved by prescribing the far-field velocity $\boldsymbol{u}^{\infty} = \dot{\mathbf{E}} \cdot \boldsymbol{x}$. For pure and simple shear simulations the strain rate tensors $\dot{\mathbf{E}}_{\text{pure}}$ and $\dot{\mathbf{E}}_{\text{simple}}$ are defined as

$$\dot{\mathbf{E}}_{\text{pure}} = \begin{bmatrix} 1 & 0 \\ 0 & -1 \end{bmatrix} \quad \text{and} \quad \dot{\mathbf{E}}_{\text{simple}} = \begin{bmatrix} 0 & 1 \\ 0 & 0 \end{bmatrix}. \tag{15}$$

As the effect of an applied strain rate is implemented by prescribing the far-field velocity, we treat the melt phase as an infinite medium, without any outer boundaries. The grain-melt boundaries are internal to this infinite melt, where continuity of velocity and stress jump boundary conditions were applied. In principle, the aggregate is similar to a dense suspension. We carried out these two sets of numerical simulations for four different values of the viscosity ratio λ (1.0, 2.0, 5.0, and 50.0) and five different values of the capillary number Ca (1, 0.7, 0.5, 0.3, 0.1, and 0.05). While the geometry of the deformed aggregates is controlled by the magnitude of strain, the viscosity ratio controls the time of deformation [*Hier-Majumder*, 2008]. To produce a high strain numerical experiment within a reasonable computation time, we employ viscosity ratios that are lower than natural values. This implies that our strain rates are higher than typical natural values. The resulting microstructure, however, is similar to what would be expected in natural aggregates with much higher viscosity ratio. We discuss this issue further in section 4.

2.3. Postprocessing

The numerical solutions to the BIE (12) and the kinematic condition (7) return the shape of each grain and the velocities at the boundary nodes of each grain at each time step. We postprocess the numerical data to calculate velocities in the interior of the grains and the melt, the differential shortening of each grain, and the contiguity tensor at each grain. In this section, we describe the method for calculating each of these quantities.

To visualize the coupled flow in the grain interior and the melt we need to construct streamlines from the velocity vectors. Once the velocities along the boundaries are known, the velocity at a point $\boldsymbol{x}_0^m$ located in the melt is computed by

$$\begin{aligned} \boldsymbol{u}(\boldsymbol{x}_0^m) = \boldsymbol{u}^{\infty}(\boldsymbol{x}_0^m) - \frac{1}{4\pi Ca} \sum_P \int_{\Gamma_P} \Delta \boldsymbol{f}(\boldsymbol{x}) \cdot \boldsymbol{\mathcal{U}}(\boldsymbol{x}, \boldsymbol{x}_0^m)\, \mathrm{d}\Gamma_P \\ + \sum_P \frac{1-\lambda_P}{4\pi} \int_{\Gamma_P} \boldsymbol{u}(\boldsymbol{x}) \cdot \boldsymbol{\mathcal{T}}(\boldsymbol{x}, \boldsymbol{x}_0^m) \cdot \hat{\boldsymbol{n}}\, \mathrm{d}\Gamma_P. \end{aligned} \tag{16}$$

Notice that in contrast to the BIE (12), the velocity $u_i(\boldsymbol{x})$ in the integrand of the double layer integral at the boundary Γ_P is now known along with the other terms on the right-hand side. Thus, by choosing the location $\boldsymbol{x}_0^m$ at various points within the melt and repeating the calculation in equation (16), we can generate the representation of the flow field within the melt.

Similarly, the velocity at a point $\boldsymbol{x}_0^g$ within the qth grain is given by

$$\begin{aligned} \boldsymbol{u}^q(\boldsymbol{x}_0^g) = \frac{1}{\lambda_q} \boldsymbol{u}^{\infty}(\boldsymbol{x}_0^g) - \frac{1}{4\pi \lambda_p Ca} \sum_P \int_{\Gamma_P} \Delta \boldsymbol{f}(\boldsymbol{x}) \cdot \boldsymbol{\mathcal{U}}(\boldsymbol{x}, \boldsymbol{x}_0^g)\, \mathrm{d}\Gamma_P \\ + \sum_P \frac{1-\lambda_P}{4\pi \lambda_q} \int_{\Gamma_P} \boldsymbol{u}(\boldsymbol{x}) \cdot \boldsymbol{\mathcal{T}}(\boldsymbol{x}, \boldsymbol{x}_0^g) \cdot \hat{\boldsymbol{n}}\, \mathrm{d}\Gamma_P. \end{aligned} \tag{17}$$

Since all quantities on the right-hand side of equation (17) are known, we can calculate the velocity within each grain by repeating the calculation for different locations $\boldsymbol{x}_0^g$ in the interior of the grain. We continue the process for other grains to compute the velocity field for a representative section of the aggregate. We generated streamlines from the known velocity fields using the visualization software Paraview.

The undeformed aggregate consists of equant, closely packed, rounded hexagonal grains with an interstitial melt. During deformation, however, the grain shapes evolve in a nonuniform manner, driven by the magnitude of the applied far-field velocity. To observe such spatial and temporal variations of grain shape, we monitor the differential shortening, D, of each grain at each time step. The differential shortening is defined as a function of the lengths of major axis (the longest measurement) L and minor axis (the shortest measurement) B of a grain,

$$D = \frac{L-B}{L+B}. \tag{18}$$

Differential shortening is zero when the grain is equant and approached the value of one as the grain flattens to a line. Unlike aspect ratio, the differential shortening measurement is bounded with $0 \leq D < 1$.

To evaluate contiguity of each grain, we first need to evaluate the contact function on the grain surface. The contact function χ is a step function, which assumes the value of unity at the grain-grain contact and zero at the grain-melt contact [*Takei*, 1998]. To evaluate the contact function, we first compute the minimum distance between a point, $\boldsymbol{x}$, on the Pth grain and all other grains as

$$d(\boldsymbol{x}) = \min_{q \neq P} \text{dist}(\boldsymbol{x}, \Gamma_q), \tag{19}$$

where $\text{dist}(\boldsymbol{x}, \Gamma_q)$ is the minimum Euclidean distance between a point $\boldsymbol{x}$ and an interface Γ_q. The contact function, $\chi(\boldsymbol{x})$, is given by

$$\chi(\boldsymbol{x}) = \begin{cases} 1 & \text{if } d(\boldsymbol{x}) < \delta \\ 0 & \text{otherwise} \end{cases}. \tag{20}$$

If the distance is less than a prescribed threshold δ, we consider the Pth grain to be in contact with another grain at the point $\boldsymbol{x}$ on the boundary.

Once the contact function is evaluated on the surface of each grain, we calculate the contiguity tensor $\boldsymbol{\psi}$

$$\boldsymbol{\psi} = \frac{1}{l} \int_{\Gamma_P} \chi(\boldsymbol{x}) \hat{\boldsymbol{n}}\hat{\boldsymbol{n}} \, \mathrm{d}\Gamma_P, \tag{21}$$

where l is the length of Γ_P [*Takei*, 1998] and $\hat{\boldsymbol{n}}$ is the unit normal on the grain surface. The physical significance of the above definition of contiguity is that it is the ratio between length of grain-grain contact over the arc length of the entire grain surface. As each grain in an aggregate can respond to the applied stresses differently, the components of the contiguity tensor can be different for each grain in the aggregate. The trace of the contiguity tensor, ψ, is also numerically evaluated at each time step for each grain.

The anisotropy of the contiguity tensor is measured by ψ_1/ψ_2 where ψ_1 and ψ_2 are the smallest and largest eigenvalues of $\boldsymbol{\psi}$, respectively. By this definition, $\psi_1/\psi_2 = 1$ when the tensor is isotropic and decreases as the anisotropy in the tensor increases.

In our formulation, undeformed intergranular contacts are treated in the limit of infinitesimally thin melt films. The derivation of the BIE requires that the continuity of velocity and the stress jump boundary conditions apply to the interface between a grain and the adjacent melt. The thickness of such a melt film, however, is smaller than the quantity δ in equation (20). Despite the theoretical presence of an infinitesimal melt film at grain-grain contacts, this technique can still be applied to model the wetting angles corresponding to different grain-grain surface tensions by prescribing appropriate variations in surface tension γ [*Hier-Majumder and Abbott*, 2010].

2.4. Numerical Methods

In this section, we briefly present the steps associated with the numerical methods involved in the solution of the BIE. To reduce the BIE into a system of algebraic equations, we discretize the BIE using the method of collocation. During discretization, the singular integrals in the BIE need to be integrated using special integration techniques. Finally, we use the fast multipole expansion to provide a fast approximation of a matrix-vector multiplication for the dense system of algebraic equations resulting from the BIE. The details of each of these steps are discussed next.

We use the method of collocation to discretize the BIE in (12). For the Pth interface, we place N_P pole nodes on the grain-melt boundary Γ_P. A segment between two poles on the boundary is referred to as a boundary element. We approximate the position within each boundary element by cubic spline interpolation [*Press et al.*, 1992]. The interfacial surface tension $\Delta f_i(\boldsymbol{x})$ and unknown velocity $u_i(\boldsymbol{x})$ along the boundary are interpolated piecewise linearly over each boundary element.

The resulting linear system is rewritten in matrix notation as

$$\left(\frac{1+\lambda}{2}\mathbf{I} - \frac{1-\lambda}{4\pi}\mathbf{T}\right)\boldsymbol{u} = \boldsymbol{u}^{\infty} - \frac{1}{4\pi Ca}\mathbf{U}\Delta\boldsymbol{f}, \tag{22}$$

where $\mathbf{I}$ is the identity matrix and the matrices $\mathbf{U}$ and $\mathbf{T}$ are generated from the kernels of the single and double layer integrals, respectively.

The method of collocation divides the interface of the Pth grain into N_P elements for which each $\boldsymbol{x}_0$ resides on at most two boundary elements. Thus, all but two of the boundary integrals on the Pth grain are regular for a given $\boldsymbol{x}_0$. Boundary integrals on the other particles are regular as well since by definition $\boldsymbol{x}_0 \notin \Gamma_q$ for $q \neq P$. These regular integrals are approximated using the eight-point Gaussian quadrature rule.

When $\boldsymbol{x}_0$ is on $\Gamma_{P,e}$, the eth boundary element on the Pth interface, the boundary integral becomes singular. For the single-layer integral, the singularity is weak meaning the integrand is still integrable despite it being unbounded. The double-layer integral has a strong singularity. Special care must be taken when numerically evaluating the integrals in both cases. A variety of techniques have been developed to evaluate singular integrals [*Pozrikidis*, 2001; *Lean and Wexler*, 1985; *Guiggiani and Gigante*, 1990; *Lachat and Watson*, 1987; *Telles*, 1987; *Gao*, 2006]. Following *Hier-Majumder* [2008], we employ the radial integration method proposed by *Gao* [2006]. The radial integration method rewrites the integral in terms of the radial distance from the singularity and approximates the integrand by a power series. The power series form allows the regular and singular portions of the integrand to be separated at which point the singular integral is analytically shown to go to zero.

The fast multipole method (FMM) uses series expansions to approximate the matrix-vector multiplications in (22). The series expansions separate the pole and field points into two separate sets of equations. This removes the requirement for a unique evaluation for every combination of pole point and boundary element. The end result is an approximate matrix-vector multiplication that takes $\mathcal{O}(N)$ time compared to $\mathcal{O}(N^2)$ time required by direct methods, where N is the total number of unknowns or the total degrees of freedom of the system of equations. The accelerated multiplication allows the use of iterative methods, such as the general minimal residual (GMRES) method [*Saad*, 2003], to solve the linear system in $\mathcal{O}(N)$ time. *Liu* [2009] presents a general discussion on fast multipole (FM) expansion for BIEs arising from various physical problems. We present the FM expansion for the single-layer integral in Appendix A.

We solved the resulting system of sparse linear equations using the GMRES method. We iterated the solver until the relative norm of the residual vector was less than 10^{-8}. As (12) is a Fredholm equation of the second type, the linear system is well conditioned and no preconditions were used. The solver converged within a maximum of 100 iterations for all geometries and values of λ and Ca presented in the paper. In our simulations, the number of GMRES iterations never reached the preset maximum of 1000 iterations.

We used an adaptive fourth-order Runge-Kutta (RK4) method to update grain shapes from equation (7) using the velocities obtained from the BIE. In this adaptive scheme, the locations of boundary nodes were updated using both one RK4 iteration of step size Δt and two RK4 iterations, each of step size $\Delta t/2$. If the L_1 norm of the difference between the pole positions for every node was less than 10^{-2}, then we used the result as the more refined evolution of the next time step. Otherwise, the process is repeated with $\Delta t/2$. When the time-stepping scheme is successful, the next evolution attempts a time step of size $2\Delta t$, as long as the new larger time step is not larger than the maximum allowed time step. Here we choose our initial and maximum time step size to be $\Delta t = 0.01$. The time stepping in our numerical code limits the simulations to small values of viscosity contrast. In the following section, we present a perturbation analysis that provides insight into the role played by viscosity contrast in the steady state shape of the grains. To validate the perturbation analysis, future work needs to incorporate an adaptive time-stepping scheme, which can adjust to variations in viscosity contrast in the numerical simulations.

The numerical solution was carried out using a Fortran 2008 library, using Intel's Math Kernel Library for linear algebra operations including the GMRES solver. The numerical results were validated against the Hadamard-Rybczyński relation for a steady state viscous drop settling in an infinite fluid [*Kim and Karilla*, 2005; *Happel and Brenner*, 1983].

2.5. Perturbation Analysis

In addition to the numerical results, we also present analytical solutions for the steady state shape of a deformed grain under an applied strain. The spherical grain is embedded in an infinite fluid. The unperturbed state is characterized by the absence of motion both within the grain and the surrounding melt. The constant surface tension γ at the grain-melt interface is balanced by the difference in constant values of pressure within the grain and the melt. In the perturbed state, we impose a straining flow on the surrounding fluid and build first-order analytical solutions for the velocities and pressures within the grain and the melt and the steady state shape of the grain as a function of the viscosity ratio, λ. A detailed description of

the methods used in building the analytical solution is provided by *Leal* [1992, chapter 5]. For brevity, we only repeat the most salient features of this analysis.

As the perturbation analysis is carried out for an isolated grain in a suspension, the contiguity of grains cannot be predicted by this technique. Despite this shortcoming, the perturbation solutions provide us with an insight into the manner in which grain shape responds to an applied external strain and the extent to which viscosity ratio modulates this response in the steady state. In this article, we follow *Leal* [1992, chapter 5] to build the first-order solutions using vector harmonics. Perturbation analyses for deformation of fluid pockets under an applied strain using vector harmonics [*Hier-Majumder*, 2011] and for variable surface tension using Lamb's solution [*Hier-Majumder*, 2008; *Hier-Majumder and Abbott*, 2010] have been presented in earlier works.

We can express the nondimensional perturbed shape of the grain by the function f as,

$$F = r - (1 + \varepsilon f) = 0, \tag{23}$$

such that the unit normal vector $\hat{\boldsymbol{n}}$ is given by

$$\hat{\boldsymbol{n}} = \frac{\boldsymbol{\nabla} F}{|\boldsymbol{\nabla} F|} = \boldsymbol{r} - \varepsilon \boldsymbol{\nabla} f. \tag{24}$$

The perturbation function f of the shape evolves following the first-order expansion of the kinematic equation (7) given by

$$\frac{\partial f}{\partial t} + \boldsymbol{u}^g \cdot \boldsymbol{r} = 0, \tag{25}$$

where $\boldsymbol{u}^g$ is the velocity at the grain boundary.

We wish to construct a set of solutions for the $\mathcal{O}(\varepsilon)$ velocities and pressures within the grain and the surrounding melt, under the action of an imposed far-field strain rate $\dot{\mathbf{E}}$, such that the mass balance and force balance equations (2) and (3) are satisfied. Since the surrounding melt extends to infinity, we also want the solutions for the melt to decay as a function of distance away from the grain. These constraints are satisfied by prescribing the following solutions for the grain interior (superscript g) and the melt (superscript m),

$$p^m = c_1 \frac{\boldsymbol{r} \cdot \dot{\mathbf{E}} \cdot \boldsymbol{r}}{r^5}, \tag{26}$$

$$\boldsymbol{u}^m = \left[1 - \frac{2c_2}{5r^5}\right] \dot{\mathbf{E}} \cdot \boldsymbol{r} + \left[\frac{c_1}{1} 2r^5 + \frac{c_2}{r^7}\right], \tag{27}$$

$$p^g = \dot{\mathbf{E}} : \left(\boldsymbol{rr} - \frac{r^2}{3}\mathbf{I}\right) d_1, \tag{28}$$

$$\boldsymbol{u}^g = \left[d_2 + \frac{5r^2}{21}\right] \dot{\mathbf{E}} \cdot \boldsymbol{r} - \frac{2d_1}{21} \boldsymbol{r} \left(\boldsymbol{r} \cdot \dot{\mathbf{E}} \cdot \boldsymbol{r}\right), \tag{29}$$

where c_i and d_i are unknown constants. Finally, we construct a solution for the shape perturbation function, f, in the following form,

$$f = b_1 \left(\boldsymbol{r} \cdot \dot{\mathbf{E}} \cdot \boldsymbol{r}\right). \tag{30}$$

To solve for the coefficients c_i and d_i, we insert these solutions into the normal and tangential components of the no-slip boundary condition (5) and the normal and tangential components of the stress jump condition (6). Matching the coefficients of each term in these substitutions, we obtain four algebraic equations which expresses the coefficients c_i and d_i in terms of b_1. Finally, we substitute the results into the linearized kinematic condition (25) to obtain the following ordinary differential equation in b_1,

$$Ca \frac{\mathrm{d}b_1}{\mathrm{d}t} = \frac{5}{2\lambda + 3} - \left[\frac{40(\lambda + 1)}{(2\lambda + 3)(19\lambda + 16)}\right] b_1. \tag{31}$$

In the steady state, the coefficient b_1 becomes

$$b_1 = \frac{19\lambda + 16}{8(\lambda + 1)}, \tag{32}$$

leading to the first-order expression for the steady state grain shape,

$$F = r - \left(1 + \varepsilon Ca \frac{19\lambda + 16}{8(\lambda + 1)} \boldsymbol{r} \cdot . \dot{\mathbf{E}} \cdot \boldsymbol{r}\right). \tag{33}$$

We discuss the implications for the results of the linear analysis in section 4.1.

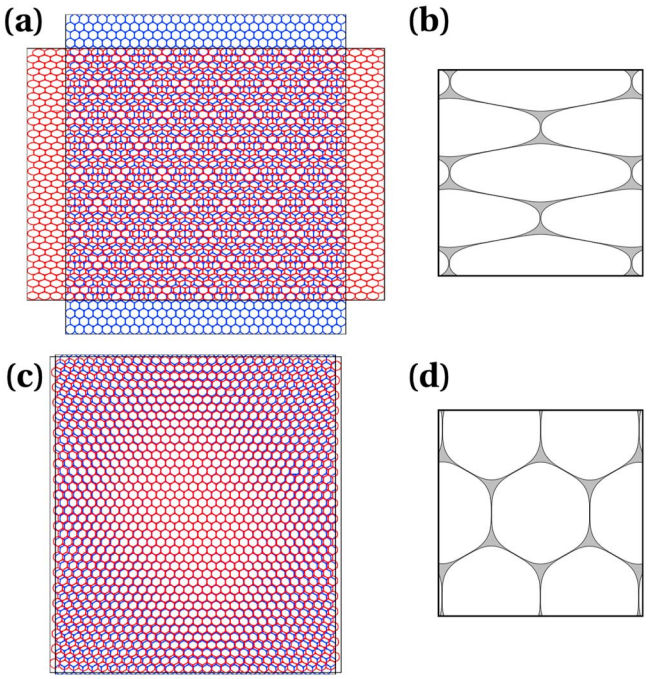

Figure 2. (a) Comparison between the deformation of a low-viscosity ratio, $\lambda = 1.0$, grain-melt aggregate at the beginning and end of a simulation in a pure shear flow. The aggregate is colored blue at the start of the evolution and red at the end. Bounding boxes are added to emphasize the overall deformation of the aggregate. (b) A sample grain-melt patch with low-viscosity ratio, $\lambda = 1.0$, at the end of a simulation in a pure shear flow. The grey areas between the grains represent the melt. (c) Comparison between the deformation of a high-viscosity ratio, $\lambda = 50.0$, grain-melt aggregate at the beginning and end of a simulation in a pure shear flow. The aggregate is colored blue at the start of the evolution and red at the end. Bounding boxes are added to emphasize the overall deformation of the aggregate. (d) A sample grain-melt patch with low-viscosity ratio, $\lambda = 50.0$, at the end of a simulation in a pure shear flow. The gray areas between the grains represent the melt.

3. Results

In this section, we present the results from our numerical simulations in pure and simple shear. Our results from both pure and simple shear simulations demonstrate that the contiguity tensor becomes strongly anisotropic with progressive deformation. We also observe that the magnitude of the differential shortening of grains is strongly anticorrelated with the anisotropy in contiguity in time and space. During pure shear deformation, melt is expelled from tubules wetting grain boundaries parallel to the principal compressive strain. During simple shear deformation, such grain boundary wetting takes place along planes oriented in a sense antithetic (at a high angle to the direction of grain elongation) to the shear direction. We elaborate these key findings in the following subsections. It is helpful to identify two descriptive components of melt geometry that will be used in the subsequent discussions. We use the term three-grain corner to identify the pocket of melt surrounded by three grains. These pockets represent cross sections of melt tubules. The value of the contact function of each of the three surrounding grains is zero in a three-grain corner. We also use the term grain boundary to indicate the region where the distance between two adjacent grains is less than the prescribed minimum distance δ. At the grain boundaries, the value of the contact function for each of the two grains is unity. The results from our microstructural analysis contain the shape and contiguity of each grain during each step of deformation, not obtainable by previous experimental and numerical techniques.

3.1. Pure Shear Deformation

When deformed in pure shear, melt from tubules in three-grain corners is expelled, wetting grain boundaries oriented parallel to the direction of principal compressive strain. The synthetic micrographs in Figure 2 demonstrate the influence of deformation on two different aggregates with different values of λ. In Figure 2a we compare the aggregates before and after deformation. In Figure 2b we display an enlarged view of the synthetic microstructure containing a few grains. Comparison between the microstructure in

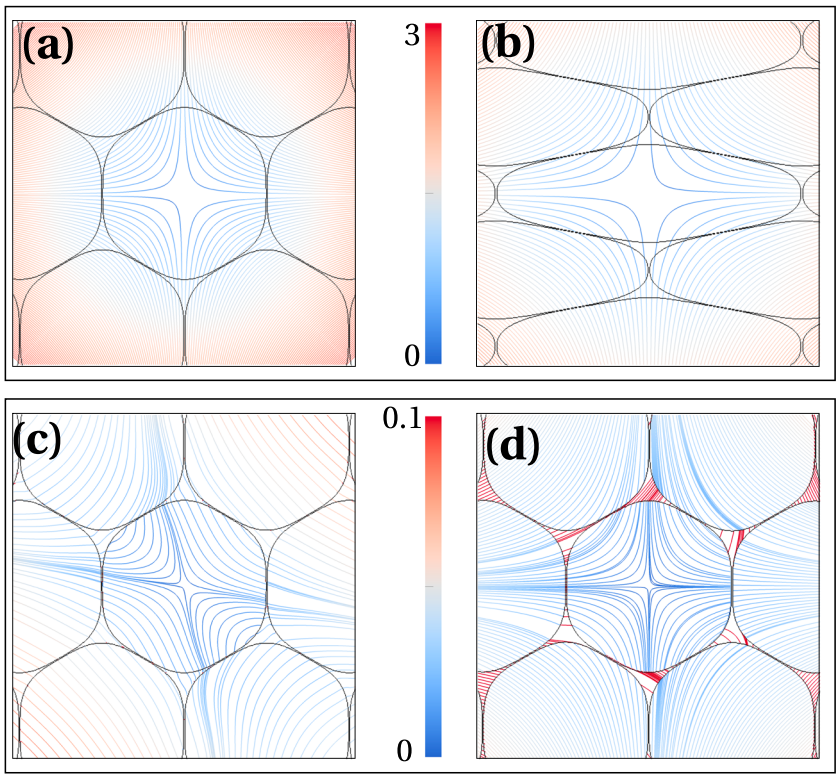

Figure 3. Streamlines indicating flow velocities within the grains and the melt pocket. Streamlines (a) at the onset and (b) at the end of the numerical experiment are drawn for $\lambda = 1$ and $Ca = 1$. Streamlines (c) at the onset of deformation and (d) at the end of deformation are drawn for $\lambda = 50$ and $Ca = 1$. The stream lines are colored by the magnitude of dimensionless velocity.

Figure 2b and the microstructure in Figure 1 reveals a few developments caused by deformation. First, the equal lengths of intergranular contact in the undeformed aggregate transformed into substantially reduced length of intergranular contact in the vertical direction in Figure 2b, while the length of intergranular contact in subhorizontal direction has increased. The distance between melt pockets along the vertical boundaries in Figure 2b is negligible, resulting in grain boundary melt films oriented along the vertical direction, which is also the direction of the principal compressive strain. This result is qualitatively similar to the experimental observations of *Daines and Kohlstedt* [1997], where they observed that initially equant melt pockets became strongly elongated along the direction of the principal compressive stress. The synthetic micrographs in Figures 2c and 2d outline the evolution of the microstructure for a higher-viscosity ratio after the same amount of computational time. For the higher-viscosity ratio aggregate, deformation and microstructural development are much less pronounced for the same length of computational time.

During deformation, the flow within the grains and the melt are strongly coupled. The synthetic micrographs in Figure 3 compare the microstructure before and after deformation for the cases discussed above. To demonstrate the nature of the coupled flow, the synthetic micrographs are overlain with streamlines colored by the magnitude of nondimensional velocity. The grain in the center of the micrographs is also located in the center of the 1200 grain aggregate. In Figures 3a and 3b streamlines continue from one grain to another and to the melt phase without distortion both before and after deformation. The small asymmetry of the streamlines in this figure is caused by numerical errors in the visualization software Paraview while calculating the streamlines from the velocity vectors. In these micrographs, the grains and the melt phase have the same viscosity and thus respond in a similar way to the imposed flow. In contrast, the flow lines display remarkable contrast between the grains and the melt phase in Figures 3c and 3d. The warmer color of the streamlines within the melt phase in Figure 3d suggests a stronger magnitude of segregation between the melt and the matrix in this case.

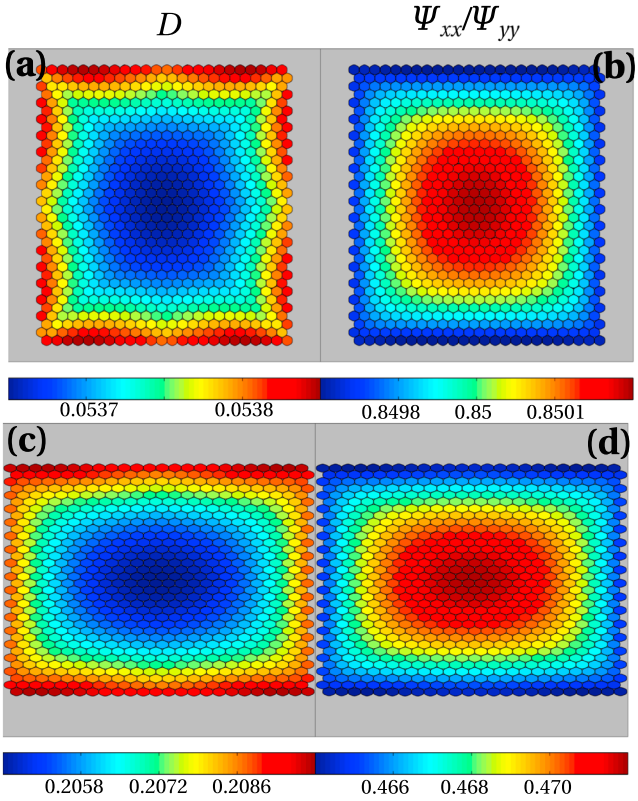

Figure 4. (a and b) Values of deformation and anisotropy in the contiguity tensor near the start, $t = 0.2$, of a simulation. (c and d) Values of deformation and anisotropy in the contiguity tensor at the end, $t = 1.0$, of a simulation. All subfigures are from a pure shear simulation with $Ca = 1.0$ and $\lambda = 1.0$. A heat map is used to show the values of grain properties for a selection of inner grains of the grain-melt aggregate. Figures 4a and 4c show the value of differential shortening, $D = (L-B)/(L+B)$, for each grain, where L is the length of the major axis and B is the length of the minor axis of the grain. Figures 4b and 4d show anisotropy of the contiguity tensor as measure by the ratio between the normal components of the contiguity tensor, ψ_1/ψ_2. The gray patches between the grains and gray area surrounding the aggregate represent the melt.

Grain deformation and the development of anisotropy in contiguity are strongly related. The synthetic micrographs in Figure 4 compare the differential shortening and the ratio between the principal components of contiguity near the beginning and the end of deformation. Comparison between the maps of D and ψ_1/ψ_2 in both undeformed and deformed states reveals that the least deformed grains, characterized by smaller values of D are also most isotropic, characterized by higher values of ψ_1/ψ_2. While the magnitude of these variations at a given state of strain are rather small, as revealed by the small range on the color scale, the pattern remains unchanged by deformation. We also notice that the average magnitude of the quantities differs substantially between Figures 4a and 4b and Figures 4c and 4d, resulting from deformation of the aggregates.

3.2. Simple Shear Deformation

In simple shear deformation, melt is expelled from the tubules to wet grain boundaries that are oriented in an antithetic sense to the applied shear strain. The synthetic micrographs in Figure 5 demonstrate the such grain boundary wetting for two different viscosity contrasts. The aggregate in Figure 5a is deformed by a dextral shear, moving the top of the aggregate to the right. The enlarged microstructure in the inset demonstrates that the grains are elongated along an axis oriented from top right to the bottom left of the window. We also notice that length of contact is substantially decreased along grain boundaries oriented in a direction perpendicular to the stretching of the grains. This observation is qualitatively similar to the experimental observations of grain boundary wetting by simple shear and torsion [*Hier-Majumder and Kohlstedt*, 2006; *King et al.*, 2011; *Zimmerman et al.*, 1999]. As observed with the pure shear case, the aggregate with the higher-viscosity contrast deformed to a much smaller extent for the same length of computational time.

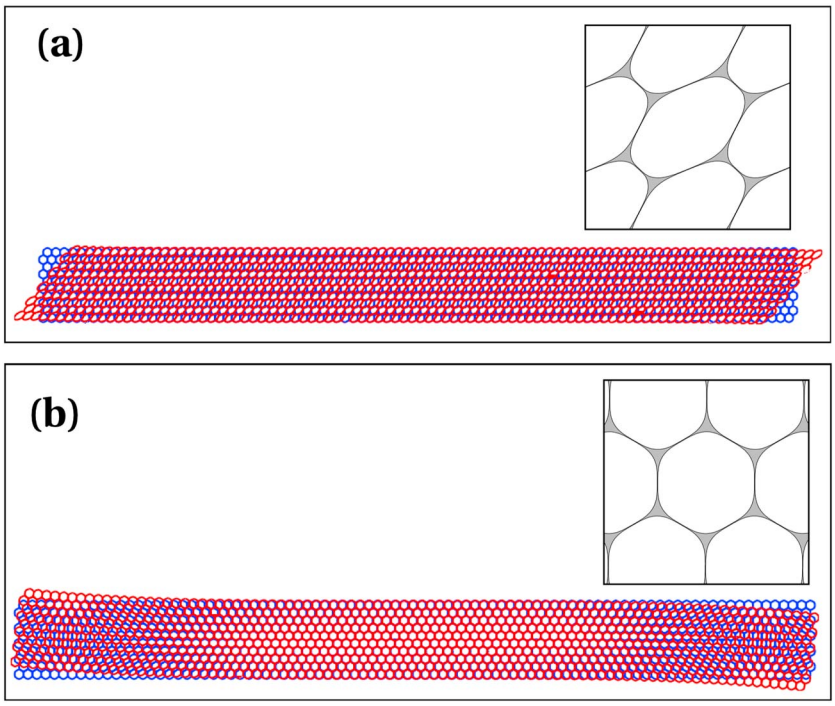

Figure 5. (a) Comparison between the deformation of a low-viscosity ratio, $\lambda = 1.0$, grain-melt aggregate at the beginning and end of a simulation in a pure shear flow. The aggregate is colored blue at the start of the evolution and red at the end. The top right portion of Figure 5a shows a sample grain-melt patch with low-viscosity ratio, $\lambda = 1.0$, at the end of a simulation in a pure shear flow. The gray areas between the grains represent the melt. (b) Comparison between the deformation of a high-viscosity ratio, $\lambda = 50.0$, grain-melt aggregate at the beginning and end of a simulation in a pure shear flow. The aggregate is colored blue at the start of the evolution and red at the end. The top right portion of Figure 5b shows a sample grain-melt patch with low-viscosity ratio, $\lambda = 50.0$, at the end of a simulation in a pure shear flow. The gray areas between the grains represent the melt.

Near the boundary of the simulated microstructures, small amounts of bulk rotation is observed. The bulk rotation is more pronounced for grains with a higher viscosity in Figure 5b. This small rotation likely arises from the response of the entire aggregate of densely packed grains to the rotational flow field imposed by simple shear. The contrast in effective viscosity of the aggregate and the suspending melt being strongest at the boundary, the rotation is confined at the boundary. Since the bulk rotation is experienced by a small fraction of the grains, contiguity averaged over the entire aggregate is still dominated by the majority of the grains in the interior which deform uniformly without bulk rotation. While a qualitatively similar behavior has been observed in dilute suspensions [*Loewenberg and Hinch*, 1996], future studies of deformation of dense clusters suspended in an infinite fluid will be beneficial to better understand the competition between bulk rotation and grain deformation. We compare our results with previous studies of simulations of suspensions in section 4.3.

Similar to the pure shear case, flow within the grains and the melt are strongly coupled in simple shear. The flow lines in Figure 6 demonstrate the nature of such coupling in an enlarged view of a few grains whose centers are aligned along the *x* axis. In all four panels, the direction of the velocity changes from the top (flowing to the right) to the bottom (flowing to the left) of the synthetic micrographs. The top two panels, Figures 6a and 6b, illustrate the development of sheared microstructure at the beginning and the end of the deformation. The streamlines continue from one grain to another and the melt without any significant bends, as all of these phases have the same viscosity. The grains in the middle row in Figure 6b develop elliptical closed loop circulation in the center in response to the reversal of the direction of the flow velocity. We do not observe any appreciable deformation of the high-viscosity grains in Figures 6c and 6d. The streamlines, however, display kinks as they move from the grains into the melt pockets. The kinks in the streamlines, similar to the pure shear case, are caused by the contrast in viscosity.

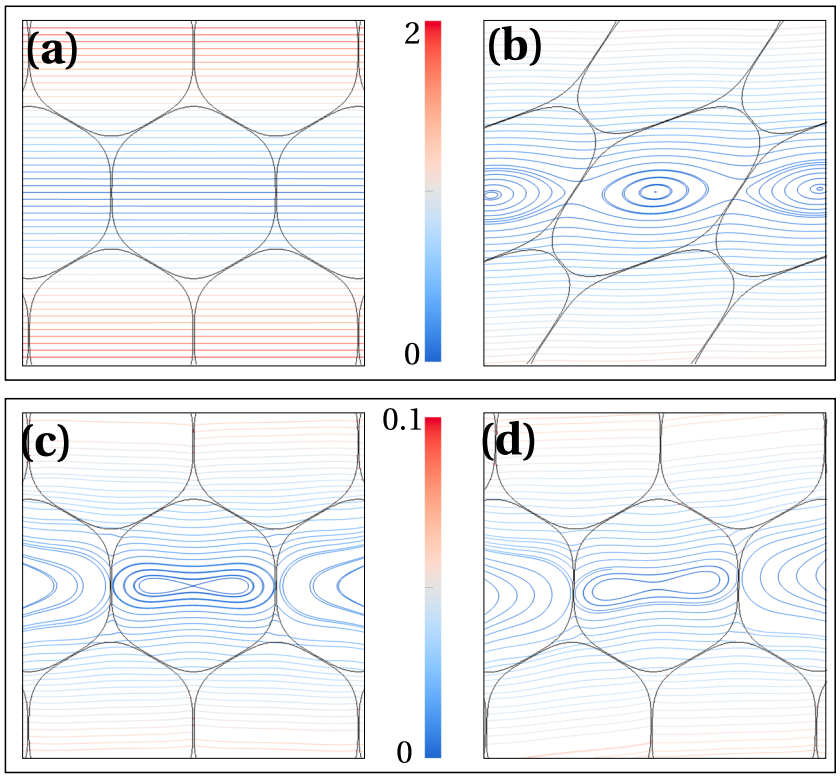

Figure 6. Streamlines indicating flow velocities within the grains and the melt pocket. Streamlines (a) at the onset and (b) at the end of the numerical experiment are drawn for $\lambda = 1$ and $Ca = 1$. Streamlines (c) at the onset of deformation and (d) at the end of deformation are drawn for $\lambda = 50$ and $Ca = 1$. The streamlines are colored by the magnitude of dimensionless velocity.

The differential shortening and anisotropy increase with an increase in the strain. The magnitude of both quantities are inversely related in space and time, as revealed by the maps in Figure 7. Figures 7a and 7b display the differential shortening D and anisotropy of contiguity, ψ_1/ψ_2 at the onset of deformation. In this state, D shows variation $\mathcal{O}(10^{-5})$ about a mean value of 0.05. After deformation, however, the mean differential shortening increases to 0.3 in Figure 7c, with the higher values concentrated near the ends. Although the $\mathcal{O}(10^{-3})$ spatial variation in the in the magnitude of D is small, the pattern is anticorrelated with the same

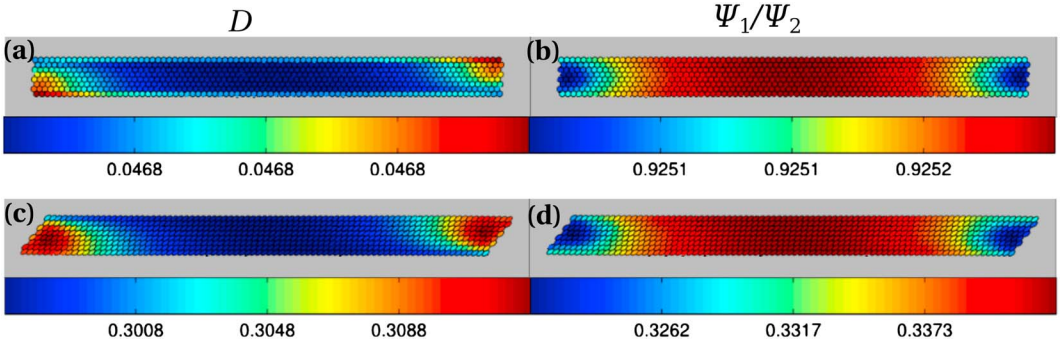

Figure 7. (a and b) Values of deformation and anisotropy in the contiguity tensor at the start, $t = 0.2$, of a simulation. (c and d) Values of deformation and anisotropy in the contiguity tensor at the end, $t = 1.0$, of a simulation. All subfigures are from a simple shear simulation with $Ca = 1.0$ and $\lambda = 1.0$. A heat map is used to show the values of grain properties for a selection of inner grains of the grain-melt aggregate. Figures 7a and 7c show the value of differential shortening, $D = (L-B)/(L+B)$, for each grain, where L is the length of the major axis and B is the length of the minor axis of the grain. Figures 7b and 7d show anisotropy of the contiguity tensor as measure by the ratio between the normal components of the contiguity tensor, ψ_1/ψ_2. The gray patches between the grains and gray area surrounding the aggregate represent the melt.

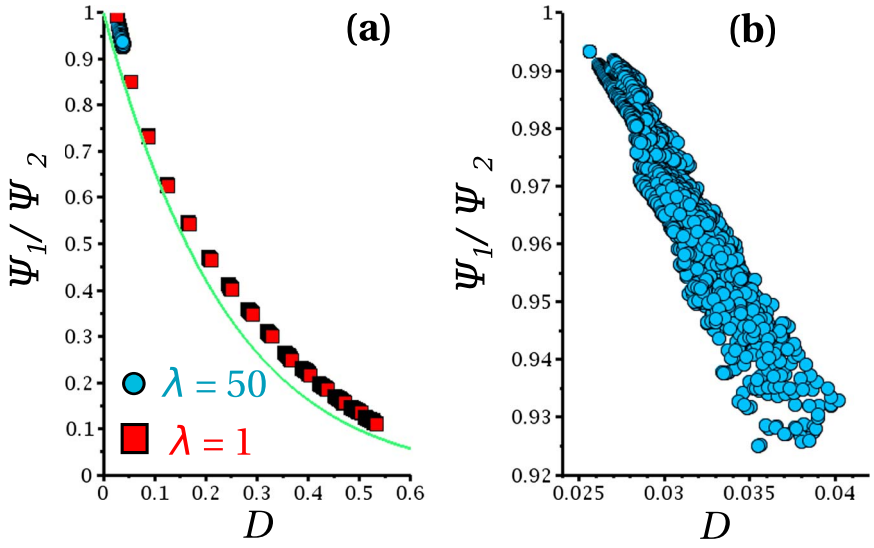

Figure 8. (a) Best fit between the anisotropy of the contiguity tensor, ψ_1/ψ_2, and differential shortening, D, for the pure shear simulations. The blue dots represent measurements of grains from simulations where $\lambda = 50.0$ and $Ca = 1.0$. The red dots represent measurements of grains from simulation where $\lambda = 1.0$ and $Ca = 1.0$. The relationship is given by $\psi_1/\psi_2 \sim \exp(-1.120D^2 - 4.096D)$ with $R^2 = 0.998$. (b) A zoomed in view of the high-viscosity data points from Figure 8a.

order of magnitude variations in the anisotropy of contiguity in Figure 7d. Notice also the sharp reduction in the average value of ψ_1/ψ_2 from 0.9 before deformation (Figure 7b) to a value of 0.3 after deformation. Similar to the observation from pure shear simulations, these results depict the grain-scale correlation between deformation and generation of anisotropic contiguity.

The negative correlation between the magnitudes of anisotropy in contiguity and differential shortening is revealed when these two quantities are continually tracked during the course of a deformation experiment. The plots in Figure 8 display this pattern. In the plots in Figure 8a, we compare the values of ψ_1/ψ_2 and D calculated from each grain at each level of shortening, from two different pure shear simulations. The plot reveals that the nature of anticorrelation is strongly nonlinear. Also, overlain on the plot is a fit to the data $\psi_1/\psi_2 = e^{-3.909D^2-1.005D}$. The plot in Figure 8b display the values for $\lambda = 50$ only. Although deformed to smaller strains, the strong negative correlation is obvious from the plot. The fact that data from both low- and high-viscosity contrast aggregates in Figure 8a follow the same trend demonstrates that the geometric parameters such as differential shortening and anisotropic contiguity are nearly insensitive to the viscosity ratio at the same stage of deformation. We discuss this issue further in the next section.

4. Discussion

4.1. Implications of the Results From Perturbation Analysis

The results from perturbation analysis provide a useful insight into the role of viscosity contrast, λ, on the steady state shape of deformed grains. The coefficient of the shape perturbation parameter, b_1, is time dependent, as revealed by equation (31). There are two terms on the right-hand side of equation (31). For a given Ca, in the limit of $\lambda \to \infty$, the first term, $5/(2\lambda + 3) \to 0$, reducing the rate of change of b_1 with time. This result simply arises from the fact that it takes longer to deform a high-viscosity grain. In a large-scale geodynamic simulation of mixing of viscous blobs in mantle flow, *Manga* [1996] noted that, for small values of λ, the time dependence of particle deformation depends weakly on λ. For the purpose of validating our numerical results, however, it is more interesting to observe the steady state behavior of the solution. In the steady state, the value of b_1 is given by the right-hand side of equation (32). This value ranges between 2 and 2.38 between the limits $\lambda \to 0$ and $\lambda \to \infty$. This narrow range of variation of b_1 with λ implies that the steady state microstructure is practically independent of the viscosity contrast between the grain and the melt. The plot in Figure 9a compares the steady state shape of a unit circle deformed under an applied pure shear strain rate in equation (15) for $\lambda = 1$ and $\lambda = 1000$. The two steady state shapes are nearly identical. The plot in Figure 9b shows the variation of b_1 with λ. The value of b_1 starts to flatten out at $\lambda = 10$ and becomes nearly constant at $\lambda = 50$. Since we are interested in simulating the steady state microstructure,

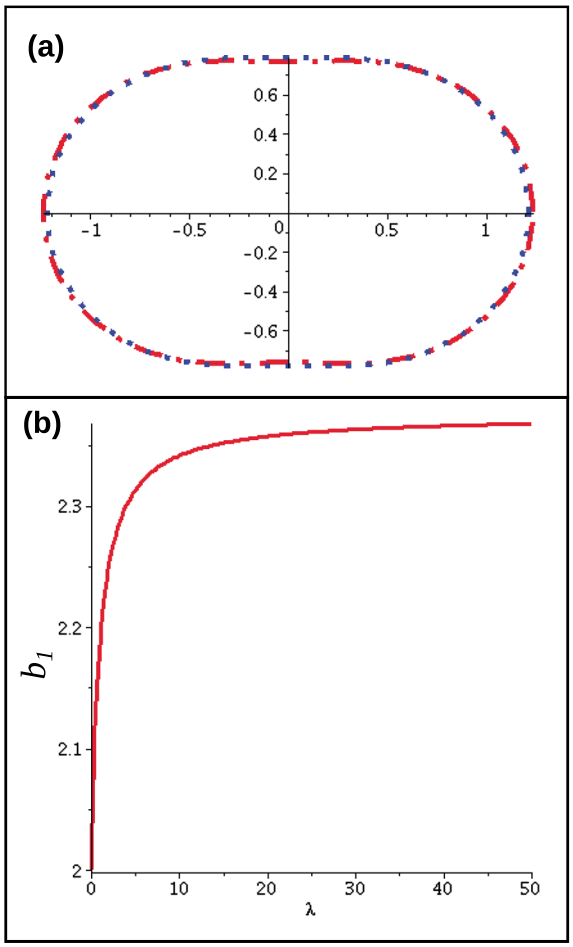

Figure 9. Results from linear analysis for $Ca = 1$ and $\varepsilon = 0.1$. (a) Steady state shape of a grain under an applied pure shear strain rate, given by equation (33) for two different values of the viscosity ratio λ. The broken blue curve corresponds to $\lambda = 1000$, and the broken red curve corresponds to $\lambda = 1$. (b) Plot of the coefficient b_1 in equation (32) as a function of the viscosity contrast λ.

this analysis provides a rationale for using the computationally inexpensive value of $\lambda = 1$, which produces a similar steady state microstructure as a computationally expensive higher-viscosity microstructure, as more time steps will be needed to achieve the steady state.

4.2. Trade-Offs in Selection of Parameters

Two key dimensionless parameters in our work are the capillary number, Ca, and the viscosity ratio, λ. The goal of our analysis is to produce a reasonable representation of steady state natural microstructure in a computationally efficient manner. The selection of the dimensionless parameters is guided by this goal. First, by slightly reordering terms, we can define the capillary number as the ratio between the applied stress and surface tension, $\sigma/(\gamma/d)$. For asthenospheric stress levels of $\sigma = 1$ kPa, natural grain size $d = 1$ mm, and interfacial tension $\gamma = 1$ J/m^2 [*Cooper and Kohlstedt*, 1982], we obtain $Ca = 1$. This value of capillary number provides a reasonable representation of natural conditions in our simulations. In laboratory experiments this trade-off is often achieved by increasing stress levels while reducing the grain size of the sample. Next, we chose the viscosity contrast $\lambda = 1$ for the majority of our simulations. As the perturbation analysis in the previous section indicates, in the first order, λ exerts a stronger influence on the rate of deformation rather than the steady state grain shape. Using a smaller value of λ, a reasonable approximation to natural microstructure can thus be simulated by taking fewer time steps to update the grain shape to steady state.

The plots in Figure 10 demonstrate the evolution of anisotropy and differential shortening with increasing strain. The plots in Figure 10a illustrate that the ratio ψ_1/ψ_2 decreases with the strain in a nonlinear fashion. The superposition of two sets of data illustrates that for a comparable strain, the influence of the viscosity contrast on the anisotropic contiguity is insignificant. The plots in Figure 10b demonstrate the differential shortening increases as the grains deform into elongated shapes with an increase in strain. As in Figure 10a, for a given strain, the influence of viscosity ratio on the differential shortening is minimal.

4.3. Comparison With Previous Results

The results from our work is in great qualitative agreement with a number of previous works. In a set of laboratory experiments, *Daines and Kohlstedt* [1997] deformed partially molten aggregates of olivine and basalt in pure shear. Studying the microstructures of the deformed samples, they observed that the initially equant melt pockets became more elongated with deformation. They also observed that these films aligned themselves in a direction parallel to the direction of principal compressive stress. This observation is similar to our synthetic micrographs where grain boundaries parallel to the principal shortening direction and perpendicular to the *x* axis are preferentially wetted resulting in elongated film-like melt units. Since the work of *Daines and Kohlstedt* [1997] did not report contiguity or differential shortening from their microstructures, direct quantitative comparison between these two works is difficult.

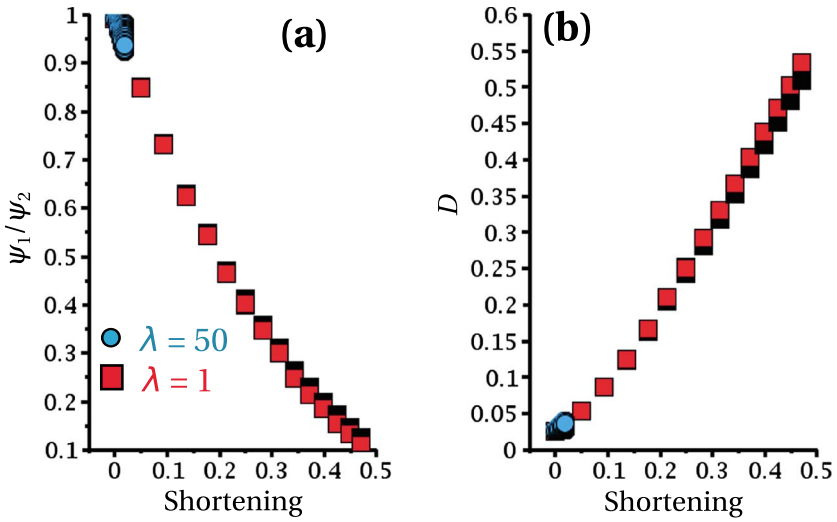

Figure 10. Development of anisotropic textures in pure shear simulations. (a) Plot of anisotropy in contiguity ψ_1/ψ_2 as a function of bulk strain for viscosity ratios $\lambda = 1$ (red squares) and $\lambda = 50$ (blue circles). (b) Plot of differential shortening as a function of bulk strain for viscosity ratios $\lambda = 1$ (red squares) and $\lambda = 50$ (blue circles).

In a set of laboratory experiments with analogue materials, *Takei* [2005] observed the development of shear wave anisotropy during deformation. The samples were deformed in pure shear configuration while alternating between the principal compressive and extensive stress. In this work, *Takei* [2005] reports average values of contiguity ψ from the deformed aggregates. The scalar contiguity, the trace of the contiguity tensor from our pure shear simulations, is similar to these reported values. We present quantitative comparisons between these two works in the companion article HMD. Qualitatively, the orientation of grain boundary films in relation to the principal compressive stress in these experiments is also similar to our pure shear simulations.

The setup of our numerical simulations is similar to those encountered in modeling microstructural development in emulsions and foams [*Loewenberg and Hinch*, 1996; *Li et al.*, 1995; *Li and Pozrikidis*, 1996; *Li et al.*, 1996]. In contrast to partially molten rocks, the densely packed matrix in foams consists of air. For isoviscous simulations, however, these results become comparable. In a two-dimensional simulation with periodic boundary conditions, *Li et al.* [1995] observe for $\lambda = 1$, $Ca > 0.1$, and an initial packing configuration similar to this work, the contact between neighboring grains become anisotropic, expelling the fluid into boundaries under tension. This observation is similar to the results reported in this article. For geologically unrealistic values of $Ca < 0.1$, strong surface tension prevents deformation of the matrix and an oscillatory pattern of grain shape evolution is observed. In initial tests of low Ca runs, we observed similar patterns. Given the values of Ca for such cases are not relevant to our simulations, we did not carry out any further tests. In a three-dimensional simulation of suspensions with 0 to 30 vol % solid grains, *Loewenberg and Hinch* [1996] studied the evolution of suspension shapes for $1 < \lambda < 5$. Their observations indicate that in the steady state, rigid body rotation of grains dominates over deformation for $\lambda > 4$. The results in Figure 10a demonstrates that at least for comparable strain we do not observe any remarkable variations in the microstructure between $\lambda = 1$ and 50. While the low solid volume fraction and geologically insignificant applied stresses in the work of *Loewenberg and Hinch* [1996] prevents a direct comparison of our results with this study, it demonstrates the need for future simulations similar to ours at high values of viscosity contrast. In this work we model the matrix as an ordered aggregate of particles. In studies of the effect of bubble concentration on the shear viscosity of lavas, *Manga et al.* [1998] and *Manga and Loewenberg* [2001] demonstrated that small differences in the effective viscosity can arise between ordered and disordered suspensions. Additionally, in this work, the matrix is composed of isoviscous grains of uniform grain size distribution. Natural aggregates can be characterized by multiple solid phases with differing grain size and differing viscosities. While we focus on the development of anisotropic fabric by segregation of melt, in future, the FMBEM formulation can be used to simulate mesoscale phenomena such as shear localization, phase segregation, and damage.

5. Conclusion

The results from our numerical simulations demonstrate that melt is expelled from grain edge tubules to grain boundary films during deformation. In pure shear configuration, the orientation of these films is parallel to the direction of the principal compressive stress. In simple shear, these films are oriented in a sense antithetic to the sense of applied shear. The results from our microgeodynamic model also demonstrate that the magnitudes of anisotropic contiguity and differential shortening display a nonlinear negative correlation. Such a correlation is revealed both in spatial distribution and in temporal evolution of these quantities with progressive deformation. We also demonstrate that the flow between the grains and the interstitial melt phase are strongly coupled during deformation.

Appendix A: Fast Multipole Method

The following is a brief overview of the mechanics for implementing FMM for the BIE in (12). Specifically, we outline the series expansions for the single-layer integral. The interested reader is encouraged to refer to *Liu and Nishimura* [2006] and *Liu* [2009] for a complete account of the derivation, technical details, and expansions for the double-layer integral.

The single-layer integral can be rewritten as complex integrals using the canonical mapping from two dimensions to the complex plane:

$$I^{(1)}_{P,e}(z_0) = \int_{\Gamma_{P,e}} \Delta f_i(z)\mathcal{U}^{*}_{i1}(z,z_0)\,\mathrm{d}\Gamma_{P,e}(z) + i\int_{\Gamma_{P,e}} \Delta f_i(z)\mathcal{U}^{*}_{i2}(z,z_0)\,\mathrm{d}\Gamma_{P,e}(z), \tag{A1}$$

where $i = \sqrt{-1}$, $z = x_1 + ix_2$. We rewrite the complex single-layer integrals in terms of the complex Green's function for the potential equation as

$$I^{(1)}_{P,e}(z_0) = \frac{1}{2}\int_{\Gamma_{P,e}} \left[\mathcal{G}(z,z_0)\Delta f(z) + \overline{\mathcal{G}(z,z_0)}\Delta f(z) - (z_0 - z)\overline{\mathcal{G}'(z_0,z)\Delta f(z)}\right]\,\mathrm{d}\Gamma_{P,e}(z), \tag{A2}$$

where $\overline{()}$ denotes the complex conjugate, $\Delta f = \Delta f_1 + i\Delta f_2$ is the complex interfacial surface tension, and the complex Green's function for the potential equation given by

$$\mathcal{G}(z,z_0) = -\ln(z_0 - z). \tag{A3}$$

The prime denotes the complex derivative with respect to the pole variable z_0. Replacing the Green's functions by a complex Taylor series, the single-layer integral becomes

$$I^{(1)}_{P,e}(z_0) = \frac{1}{2}\left[\sum_{k=0}^{\infty} O_k(z_0 - z_c)M_k(z_c) + z_0\sum_{k=0}^{\infty}\overline{O_{k+1}(z_0 - z_c)M_k(z_c)} + \sum_{k=0}^{\infty}\overline{O_k(z_0 - z_c)}N_k(z_c)\right], \tag{A4}$$

with series coefficients

$$M_k(z_c) = \int_{\Gamma_{P,e}} I_k(z - z_c)\Delta f(z)\,\mathrm{d}\Gamma_{P,e}(z), \quad \text{for } k \geq 0 \tag{A5}$$

$$N_0(z_c) = \int_{\Gamma_{P,e}} \Delta f(z)\,\mathrm{d}\Gamma_{P,e}(z) \tag{A6}$$

$$N_k(z_c) = \int_{\Gamma_{P,e}} \left[\overline{I_k(z - z_c)}\Delta f(z) - z\overline{I_{k-1}(z - z_c)\Delta f(z)}\right]\,\mathrm{d}\Gamma_{P,e}(z), \quad \text{for } k \geq 1, \tag{A7}$$

which use the auxiliary functions

$$I_k(z) = \frac{z^k}{k!}, \quad \text{for } k \geq 0 \tag{A8}$$

and

$$O_0(z) = -\ln(z) \quad \text{and} \quad O_k(z) = \frac{(k-1)!}{z^k}, \quad \text{for } k \geq 1. \tag{A9}$$

The series (A4) is commonly referred to as a "far-field" expansion since it is only valid when $|z-z_c| \ll |z_c-z_0|$, which is to say the pole point is located much farther way from the expansion center than the field points on the boundary element. The far-field series coefficients only depend on the boundary element $\Gamma_{P,e}$ and expansion center z_c. Once the coefficients are computed, the series (A4) only depends on the pole point and expansion center. In this way the pole point is separated from the boundary elements with the field points absorbed the far-field coefficients $M_k(z_c)$ and $N_k(z_c)$. As with traditional series, far-field series that are expanded about the same point but representing different boundary integrals can be merged by adding coefficients. Furthermore, the series can be translated from z_c to a new expansion center z_c' under the addition condition that $|z - z_c'| \ll |z_c' - z_0|$.

The FMM uses near-field expansions, $L(z_L)$ and $K(z_L)$, centered about z_L to further merge far-field series. The near-field coefficients are constructed from far-field coefficients. As the name implies, near-field series are only valid when $|z_0 - z_L| \ll |z_c - z_L|$, which is to say that the pole point must be much closer to the near-field expansion center than the expansion center of the far-field series expansion. Like the far-field series, near-field series can be translated from z_L to z_L'. The near-field expansions are related to the boundary element integrals through

$$\sum_{e\in E} I_e^{(1)}(z_0) = \frac{1}{2}\left[\sum_{l=0}^{\infty} L_l(z_L) I_l(z_0 - z_L) - z_0 \sum_{l=1}^{\infty} \overline{L_{(}z_L) I_{l-1}(z_0 - z_L)} + \sum_{l=0}^{\infty} K_l(z_L)\overline{I_l(z_0 - z_L)}\right], \tag{A10}$$

where E is the set of the boundary elements sufficiently far and z_0.

We partition the computational domain using the Morton numbering scheme to aid with the creation, translation, and combination of series coefficients. The Morton numbering scheme partitions the domain into nested square cells based on an index generated from the cell's position in the physical domain. A typical cell has a parent, neighbors, and child cells, all of which can be computed in $\mathcal{O}(1)$ time given the Morton number of the cell. Cells with no children are commonly referred to as leaf cells.

Initially, far-field expansions are expanded about the center of each left cell. At this stage the series for a leaf cell represents only the boundary integral over the elements in that cell. Far-field expansions are translated to the center of their parent cell in the upward pass of the algorithm. After all cells have a far-field series, they are converted to near-field series and translated down to child cells in the downward pass until all leaf nodes have a near-field expansion. The final near-field series expansions in a leaf cell represent the boundary integrals over all of the boundary elements located sufficiently far from the leaf cell. The process for creating the near-field series takes $\mathcal{O}(N)$ time and storage [*Liu and Nishimura*, 2006; *Liu*, 2009].

The result of the upward and downward pass is a near-field series in each leaf cell representing $\mathcal{O}(N)$ of the boundary element integrals. The series are evaluated quickly, only relying on the pole point, expansion center, and near-field coefficients. There are $\mathcal{O}(1)$ integrals not represented by the each near-series, which must be computed directly. With the series and direct evaluation taking $\mathcal{O}(1)$ time to compute for each cell, evaluating the integrals for all poles requires $\mathcal{O}(N)$ time. In all, the FMM reduces the time to perform a matrix-vector multiplication from $\mathcal{O}(N^2)$ time and storage to $\mathcal{O}(N)$.

The low cost of the matrix-vector multiplication in conjunction with the stability provided by the BIE being a Fredholm equation of the second type allows the use of iterative solution methods like the general minimal residual method. With FMM, the BIE can be solved for large numbers of pole points using a feasible amount of computing resources.

Acknowledgments
The work in this paper has been supported by an NSF grant EAR 1215800. We are grateful to Michael Manga and an anonymous reviewer for providing insightful comments that greatly helped improve the manuscript. In compliance with the AGU data policy, the data required to produce the results of this paper can be requested from the corresponding author by formal written communication.

References

Beghein, C., K. Yuan, N. Schmerr, and Z. Xing (2014), Changes in seismic anisotropy shed light on the nature of the Gutenberg discontinuity, *Science*, *343*, 1237–40.

Cooper, R. F., and D. L. Kohlstedt (1982), *High Pressure Research in Geophysics, Advances in Earth and Planetary Sciences*, chap. Interfacial Energies in Olivine-Basalt System, Cent. Acad. Pub., Tokyo, Japan.

Daines, M. J., and D. L. Kohlstedt (1997), Influence of deformation in melt topology in peridotites, *J. Geophys. Res.*, *102*, 10,257–10,271.

Evans, R. L., G. Hirth, K. Baba, D. Forsyth, A. Chave, and R. Mackie (2005), Geophysical evidence from the MELT area for compositional controls on oceanic plates, *Nature*, *437*, 249–52.

Fischer, K. M., H. A. Ford, D. L. Abt, and C. A. Rychert (2010), The lithosphere-asthenosphere boundary, *Annu. Rev. Earth Planet. Sci.*, *38*, 551–575.

Gao, X.-W. (2006), Numerical evaluation of singular boundary integrals—Theory and Fortran code, *J. Comput. Appl. Math.*, *188*, 44–64.

German, R. (1985), *Liquid Phase Sintering*, Plenum Press, New York.

Guiggiani, M., and A. Gigante (1990), A general algorithm for multidimensional cauchy principal value integrals in the boundary element method, *ASME J. Appl. Mech.*, *57*, 906–915.
Happel, J., and H. Brenner (1983), *Low Reynolds Number Hydrodynamics*, Springer, Netherlands.
Hier-Majumder, S. (2008), Influence of contiguity on seismic velocities of partially molten aggregates, *J. Geophys. Res.*, *113*, B12205, doi:10.1029/2008JB005662.
Hier-Majumder, S. (2011), Development of anisotropic mobility during two-phase flow, *Geophys. J. Int.*, *186*, 59–68.
Hier-Majumder, S., and M. E. Abbott (2010), Influence of dihedral angle on the seismic velocities in partially molten rocks, *Earth Planet. Sci. Lett.*, *299*, 23–32.
Hier-Majumder, S., and T. Drombosky (2015), Development of anisotropic contiguity in deforming partially molten aggregates: 2. Implications for the lithosphere-asthenosphere boundary, *J. Geophys. Res. Solid Earth*, *120*, 764–777, doi:10.1002/2014JB011454.
Hier-Majumder, S., and D. Kohlstedt (2006), Role of dynamic grain boundary wetting in fluid circulation beneath volcanic arcs, *Geophys. Res. Lett.*, *33*, L08305, doi:10.1029/2006GL025716.
Holtzman, B. K., D. L. Kohlstedt, M. E. Zimmerman, F. Heidelbach, T. Hiraga, and J. Hustoft (2003), Melt segregation and strain partitioning: Implications for seismic anisotropy and mantle flow, *Science*, *301*, 1227–1230.
Hustoft, J., and D. Kohlstedt (2006), Metal-silicate seggregation in deforming dunitic rocks, *Geochem. Geophys. Geosyst.*, *7*, Q02001, doi:10.1029/2005GC001048.
Kang, S.-J. L. (2005), *Sintering: Densification, Grain Growth and Microstructure*, Elsevier, Oxford, U. K.
Kim, S., and S. J. Karilla (2005), *Microhydrodynamics: Principles and Selected Applications*, chap. 13, Dover, The Univ. of Michigan.
King, D. S. H., S. Hier-Majumder, and D. L. Kohlstedt (2011), An experimental study of the effects of surface tension in homogenizing perturbations in melt fraction, *Earth Planet. Sci. Lett.*, *307*, 735–749.
Lachat, J., and J. Watson (1987), Effective numerical treatment of boundary integral equations: A formulation for three-dimensional elastostatics, *Int. J. Numer. Methods Eng.*, *10*, 991–1005.
Ladyzhenskaya, O. (1963), *The Mathematical Theory of Viscous Incompressible Flow*, chap. 3, Gordon and Breach, The Univ. of Michigan.
Leal, G. (1992), *Laminar Flow and Convective Transport Processes*, Butterworth-Heinemann, The Univ. of Michigan.
Lean, M., and A. Wexler (1985), Accurate numerical integration of singular boundary element kernels over boundaries with curvature, *Int. J. Numer. Methods Eng.*, *21*, 211–228.
Li, X., and C. Pozrikidis (1996), Shear flow over a liquid drop adhering to a solid surface, *J. Fluid Mech.*, *307*, 167–190.
Li, X., H. Zhou, and C. Pozrikidis (1995), A numerical study of the shearing motion of emulsions and foams, *J. Fluid Mech.*, *286*, 379–404.
Li, X., R. Charles, and C. Pozrikidis (1996), Simple shear flow of suspension of liquid drops, *J. Fluid Mech.*, *320*, 395–416.
Liu, Y. (2009), *Fast Multipole Boundary Element Method*, Cambridge Univ. Press, Cambridge, U. K.
Liu, Y., and N. Nishimura (2006), The fast multipole boundary element method for potential problems: A tutorial, *Eng. Anal. Boundary Elem.*, *30*, 371–381.
Loewenberg, M., and E. J. Hinch (1996), Numerical simulation of a concentrated emulsion in shear flow, *J. Fluid Mech.*, *321*, 395–419.
Manga, M. (1996), Mixing of heterogeneities in the mantle: Effect of viscosity differences, *Geophys. Res. Lett.*, *23*, 403–406.
Manga, M., and M. Loewenberg (2001), Viscosity of magmas containing highly deformable bubbles, *J. Volcanol. Geotherm. Res.*, *105*, 19–24.
Manga, M., and H. Stone (1993), Buoyancy-driven interactions between two deformable viscous drops, *J. Fluid Mech.*, *256*, 647–683.
Manga, M., J. Castro, K. V. Cashman, and M. Loewenberg (1998), Rheology of bubble-bearing magmas, *J. Volcanol. Geotherm. Res.*, *87*, 15–28.
Naif, S., K. Key, S. Constable, and R. L. Evans (2013), Melt-rich channel observed at the lithosphere-asthenosphere boundary, *Nature*, *495*, 356–359.
Nettles, M., and A. M. Dziewoński (2008), Radially anisotropic shear velocity structure of the upper mantle globally and beneath North America, *J. Geophys. Res.*, *113*, B02303, doi:10.1029/2006JB004819.
Pozrikidis, C. (2001), Interfacial dynamics for Stokes flow, *J. Comput. Phys.*, *169*, 250–301.
Press, W. H., S. A. Teukolsky, W. T. Vetterling, and B. P. Flannery (1992), *Numerical Recipes in Fortran*, 2nd ed., chap. 19.6, Cambridge Univ. Press, Cambridge, U. K.
Rychert, C. A., P. M. Shearer, and K. M. Fischer (2010), Scattered wave imaging of the lithosphere-asthenosphere boundary, *Lithos*, *120*, 173–185.
Saad, Y. (2003), *Iterative Methods for Sparse Linear Systems*, 2nd ed., SIAM, Philadelphia, Pa.
Schmerr, N. (2012), The Gutenberg discontinuity: Melt at the lithosphere-asthenosphere boundary, *Science*, *335*, 1480–1483.
Sifré, D., E. Gardés, M. Massuyeau, L. Hashim, S. Hier-Majumder, and F. Gaillard (2014), Electrical conductivity during incipient melting in the oceanic low-velocity zone, *Nature*, *509*(7498), 81–85, doi:10.1038/nature13245.
Takei, Y. (1998), Constitutive mechanical relations of solid-liquid composites in terms of grain boundary contiguity, *J. Geophys. Res.*, *103*, 18,183–18,203.
Takei, Y. (2005), Deformation-induced grain boundary wetting and its effect on accoustic and rheological properties of partially molten rock analogue, *J. Geophys. Res.*, *110*, B12203, doi:10.1029/2005JB003801.
Takei, Y., and B. K. Holtzman (2009), Viscous constitutive relations of solid-liquid composites in terms of grain boundary contiguity: 3. Causes and consequences of viscous anisotropy, *J. Geophys. Res.*, *114*, B06207, doi:10.1029/2008JB005852.
Telles, J. (1987), A self-adaptive coordinate transformation for efficient numerical evaluation of general boundary element integrals, *Int. J. Numer. Methods Eng.*, *24*, 959–973.
von Bargen, N., and H. Waff (1986), Permeabilities, interfacial areas and curvatures of partially molten systems: Results of numerical computations of equilibrium microstructures, *J. Geophys. Res.*, *91*, 9261–9276.
Wimert, J. T., and S. Hier-Majumder (2012), A three-dimensional microgeodynamic model of melt geometry in the Earth's deep interior, *J. Geophys. Res.*, *117*, B04203, doi:10.1029/2011JB009012.
Wray, P. J. (1976), The geometry of two-phase aggregates in which the shape of the second phase is determined by its dihedral angle, *Acta Metall.*, *24*, 125–135.
Zimmerman, M. E., S. Zhang, D. L. Kohlstedt, and S.-I. Karato (1999), Melt distribution in mantle rocks deformed in shear, *Geophys. Res. Lett.*, *26*, 1505–1508.